Contents

Outline

- Angle Domain Common Image Gathers (ADCIGs)
  - ADCIGs before imaging (2-D and 3-D)
  - ADCIGs after imaging (2-D and 3-D)
- ADCIGs and velocity errors
  - Image-point movement caused by velocity errors
  - 3-D Residual Moveout in angle domain
- Aliasing in prestack wave-equation migration
  - Operator aliasing in wavefield-continuation migration
  - Shot decimation in stack and ADCIGS
  - Aliasing and velocity estimation

Outline

- Angle Domain Common Image Gathers (ADCIGs)
  - ADCIGs before imaging (2-D and 3-D)
  - ADCIGs after imaging (2-D and 3-D)
- ADCIGs and velocity errors
  - Image-point movement caused by velocity errors
  - 3-D Residual Moveout in angle domain
- Aliasing in prestack wave-equation migration
  - Operator aliasing in wavefield-continuation migration
  - Shot decimation in stack and ADCIGS
  - Aliasing and velocity estimation

The image is then obtained by extracting the values of the wavefield at zero time. The usual migration process can be schematically represented as follows:

$$P(\omega, \mathbf{m}, \mathbf{h}; z=0) \overset{\text{DSR}}{\Longrightarrow} P(\omega, \mathbf{m}, \mathbf{h}; z) \tag{1.1}$$

$$P(\omega, \mathbf{m}, \mathbf{h}; z) \overset{Imaging}{\Longrightarrow} P(t=0, \mathbf{m}, \mathbf{h}; z). \tag{1.2}$$

To compute ADCIGs, we need to introduce a slant-stack transformation between downward continuation [step (1.1)] and imaging [step (1.2)]. The results of slant stacks are functions of the offset ray parameter $\mathbf{p_h}$ and the intercept time τ. The image is then obtained by extracting the values of the wavefield at zero intercept time; i.e. $\tau = 0$. The migration process used to produce ADCIGs can be schematically represented as follows:

$$P(\omega, \mathbf{m}, \mathbf{h}; z=0) \overset{\text{DSR}}{\Longrightarrow} P(\omega, \mathbf{m}, \mathbf{h}; z) \tag{1.3}$$

$$P(\omega, \mathbf{m}, \mathbf{h}; z) \overset{Slant\ stack}{\Longrightarrow} P(\tau, \mathbf{m}, \mathbf{p_h}; z) \tag{1.4}$$

$$P(\tau, \mathbf{m}, \mathbf{p_h}; z) \overset{Imaging}{\Longrightarrow} P(\tau=0, \mathbf{m}, \mathbf{p_h}; z). \tag{1.5}$$

Figure 1.1 illustrates the subsequent stages of the process represented in (1.3–1.5).

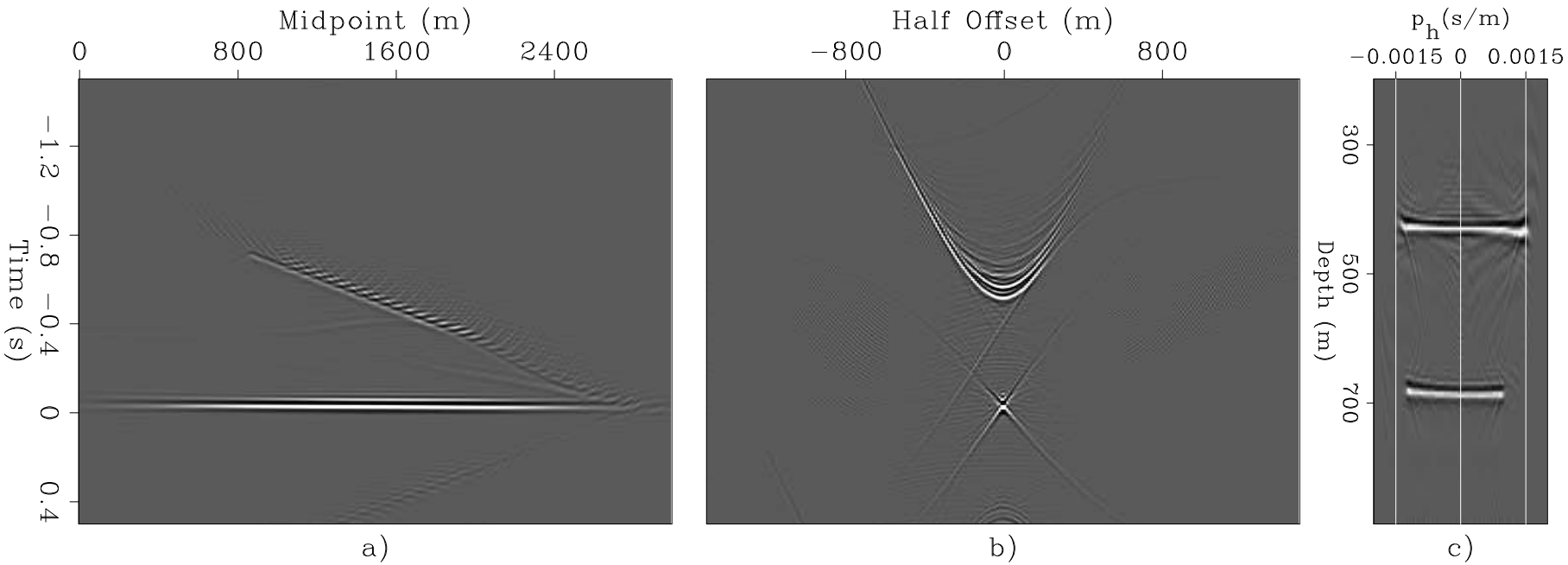

Figure 1.1: Illustration of the method for computing ADCIGs before imaging. Orthogonal slices of the prestack wavefield after downward continuation with the correct velocity to the depth of 700 meters; that is, the depth of the flat reflector: zero-offset section (panel a), and the common-midpoint gather at 1,410 meters (panel b). Panel c) shows the complete (i.e. for all depths) ADCIG at 1,410 meters. cig-zoff-cmp-cig-dip-overn-z700 [CR,M]

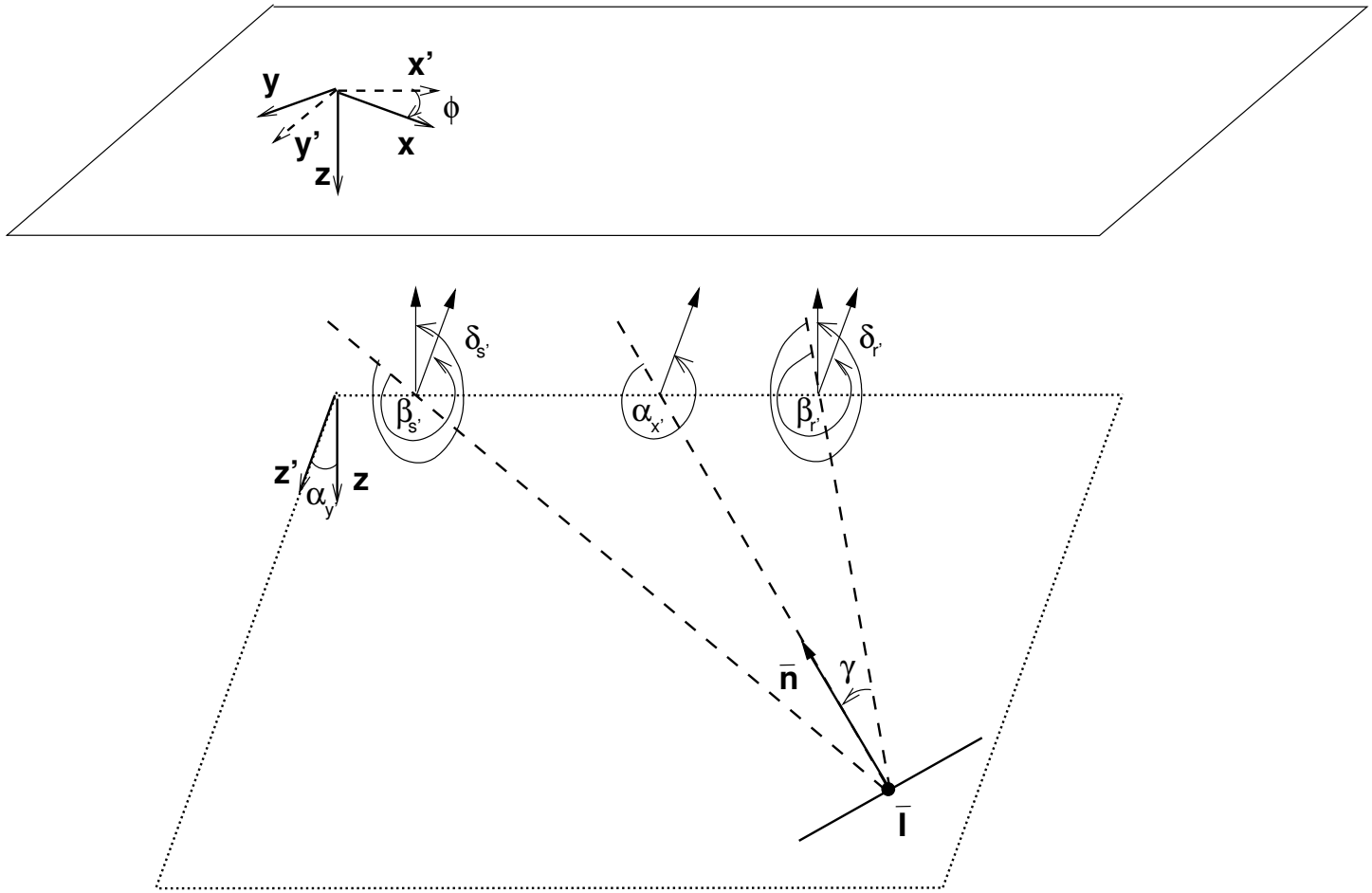

Figure 1.4: A schematic of the geometry of an angle-domain CIG gather in 3-D. The geometry is analogous to the 2-D case illustrated in Figure **??**. In contrast with the schematic of Figure **??**, the plane of coplanarity is not vertical but it is tilted by $\alpha_{y'}$ and rotated by ϕ with respect to the horizontal coordinates. cig-cig-3d-v4 [NR]

According to equation (**??**), the offset ray parameter can be expressed as a function of the source and receiver ray parameters (p_{x_s}, p_{x_g}) as follows:

$$p_{x_h} = p_{x_g} - p_{x_s}. \tag{1.6}$$

The source and receiver ray parameters (p_{x_s}, p_{x_g}) are functions of the source and receiver ray propagation angles (β_s, β_r) and of the velocity at the reflector $v(z,x)$ as follows:

$$p_{x_s} = \frac{\sin\beta_s}{v(z,x)} \quad \text{and} \quad p_{x_g} = \frac{\sin\beta_r}{v(z,x)}. \tag{1.7}$$

Substituting the relationships in (1.7) into equation (1.6), then using the angular relationship expressed in equation (**??**) and applying fundamental trigonometric identities, we obtain the desired relationship:

$$p_{x_h} = \frac{\sin\beta_r - \sin\beta_s}{v(z,x)} = \frac{2\sin\left(\frac{\beta_r-\beta_s}{2}\right)\cos\left(\frac{\beta_r+\beta_s}{2}\right)}{v(z,x)} = \frac{2\sin\gamma\cos\alpha_x}{v(z,x)}, \tag{1.8}$$

which directly links the offset ray parameter p_{x_h} to the reflection opening angle γ. The mapping of the p_{x_h} axis into the γ axis depends on both the local velocity and the geological dip. When the spatial velocity variations are significant and the

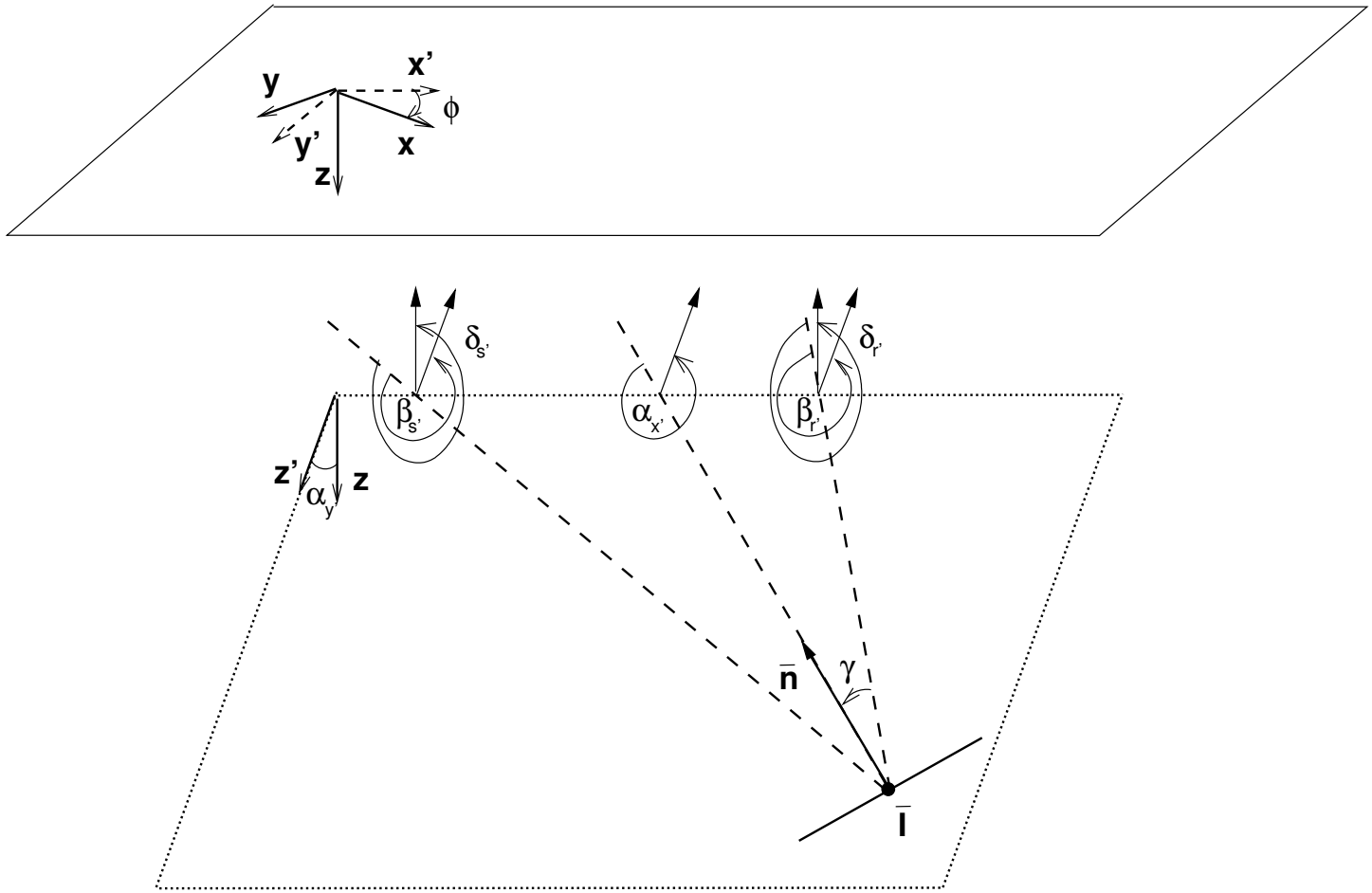

Figure 1.4: A schematic of the geometry of an angle-domain CIG gather in 3-D. The geometry is analogous to the 2-D case illustrated in Figure **??**. In contrast with the schematic of Figure **??**, the plane of coplanarity is not vertical but it is tilted by $\alpha_{y'}$ and rotated by ϕ with respect to the horizontal coordinates. cig-cig-3d-v4 [NR]

$p_{x's}, p_{y's}, p_{x'g}, p_{y'g}$ must be related by the following expression:

$$\left(p_{y'g} - p_{y's}\right) = \left(p_{y'g} + p_{y's}\right) \frac{\sqrt{\frac{1}{v^2(\mathbf{g}',z)} - p_{x'g}^2} - \sqrt{\frac{1}{v^2(\mathbf{s}',z)} - p_{x's}^2}}{\sqrt{\frac{1}{v^2(\mathbf{g}',z)} - p_{x'g}^2} + \sqrt{\frac{1}{v^2(\mathbf{s}',z)} - p_{x's}^2}}. \tag{1.9}$$

This relationship was derived by Biondi and Palacharla (1996) to define common-azimuth migration, and it is demonstrated in the Appendix of their paper.

Using the relationships among the ray parameters expressed in equations (**??**) and the relationships between the ray parameters and the angles expressed in equations (1.7), and after applying trigonometric identities, we can rewrite equation (1.9) as follows:

$$p_{y'h} = \frac{\sin\alpha_{y'}\left(\cos\beta_r - \cos\beta_s\right)}{v\left(z',x',y'\right)\left(\cos\beta_r + \cos\beta_s\right)} = -\frac{\sin\alpha_{y'}\tan\gamma\tan\alpha_{x'}}{v\left(z',x',y'\right)}. \tag{1.10}$$

The in-line offset ray parameter from equation (1.8) can also be rotated by the azimuth ϕ to give the following expression:

$$p_{x'h} = \frac{2\sin\gamma\cos\alpha_{x'}}{v\left(z',x',y'\right)}, \tag{1.11}$$

- **ADCIG after imaging in 2-D – ADCIG(γ)**

The application of the imaging condition transforms a wavefield propagating in time into an image cube that is function of depth. The transformation from time to depth depends on the local dips in the wavefield and the local propagation velocity. In the frequency-wavenumber domain this transformation is represented by the DSR operator, which in 2-D can be expressed as a function of the angles β_s and β_r as follows:

$$k_z = -\frac{\omega}{v(z,x)}(\cos\beta_r + \cos\beta_s). \tag{1.12}$$

Recalling the relationship between the in-line offset wavenumber k_{x_h} and the in-line offset ray parameter p_{x_h}:

$$k_{x_h} = p_{x_h}\omega, \tag{1.13}$$

and substituting both equation (1.12) and equation (1.8) in equation (1.13), we obtain the following relationship:

$$k_{x_h} = -p_{x_h}\frac{k_z v(z,x)}{\cos\beta_r + \cos\beta_s} = -\frac{2\sin\gamma\cos\alpha_x}{v(z,x)}\frac{k_z v(z,x)}{2\cos\gamma\cos\alpha_x} = -k_z\tan\gamma. \tag{1.14}$$

This relationship directly links the dips in the depth-offset domain $\left(k_{x_h}/k_z\right)$ to the aperture angle ($\tan\gamma$). Notice that both the local velocity $v(z,x)$ and the in-line dip

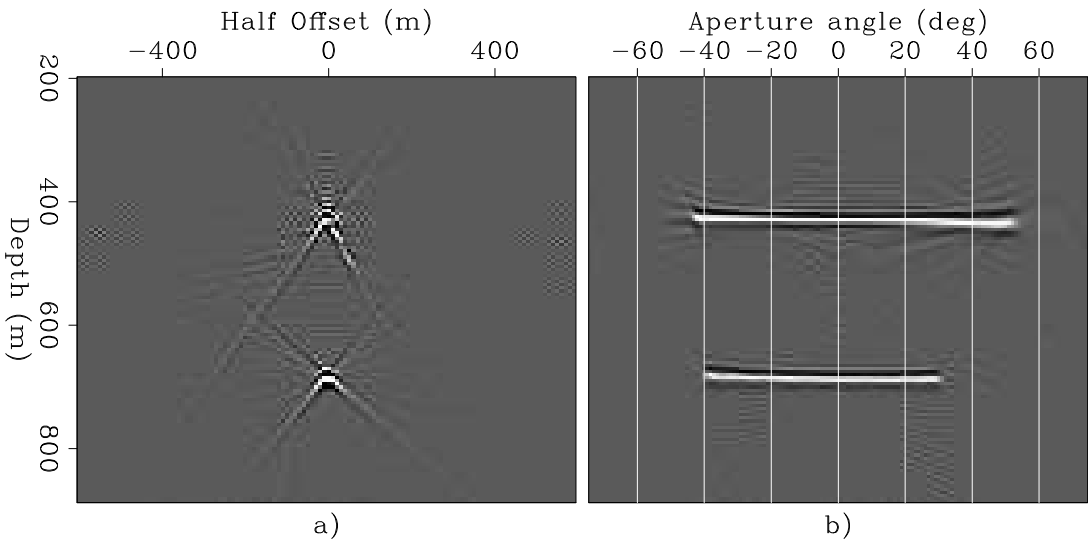

Figure 1.5: ODCIG (panel a) and ADCIG(γ) (panel b) after migration with the correct velocity. These CIGs are taken from the same data and at the same surface location as the ADCIG shown in Figure 1.1c. cig-off-ang-cig-dip-overn-dz5 [CR,M]

- **ADCIG after imaging in 3-D – ADCIG(γ, ϕ)**

The vertical wavenumber $k_{z'}$ is thus related to the vertical wavenumber k_z as follows: $k_{z'} = k_z \cos\alpha_{y'} = \sqrt{k_z^2 + k_{y'}^2}$. Substituting this relationship into equation (1.14) leads to its 3-D equivalent:

$$k_{x'_h} = -k_{z'} \tan\gamma = -\sqrt{k_z^2 + k_{y'}^2} \tan\gamma. \tag{1.15}$$

This 3-D expression is not independent of the geological dips as was its 2-D equivalent [equation (1.14)]. When deriving the after-imaging equivalent of equation (1.10), we need to take into account that $\alpha_{x'}$ is also measured along the tilted axis and thus that $\tan\alpha_{x'} = -k_{x'}/k_{z'}$. Using equation (1.10) and equation (1.15) we derive the following relationship, which expresses $k_{y'_h}$ as a function of the other wavenumbers in the image:

$$k_{y'_h} = -k_{y'} \tan\gamma \tan\alpha_{x'} = -\frac{k_{y'} k_{x'_h} k_{x'}}{{k_{z'}}^2} = -\frac{k_{y'} k_{x'_h} k_{x'}}{k_z^2 + k_{y'}^2}. \tag{1.16}$$

The combination of equation (1.15) and equation (1.16) enables the computation of 3-D ADCIGs after imaging; using these two relationships, we can map the prestack

Figure 1.9: Reflectors' geometry for the synthetic data set used to illustrated 3-D ADCIGs. The reflectors are slanted planes, dipping at 0°, 15°, 30°, 45° and 60° toward increasing x and y; they are oriented with an azimuth of 45° with respect to the in-line direction. cig-planes [NR]

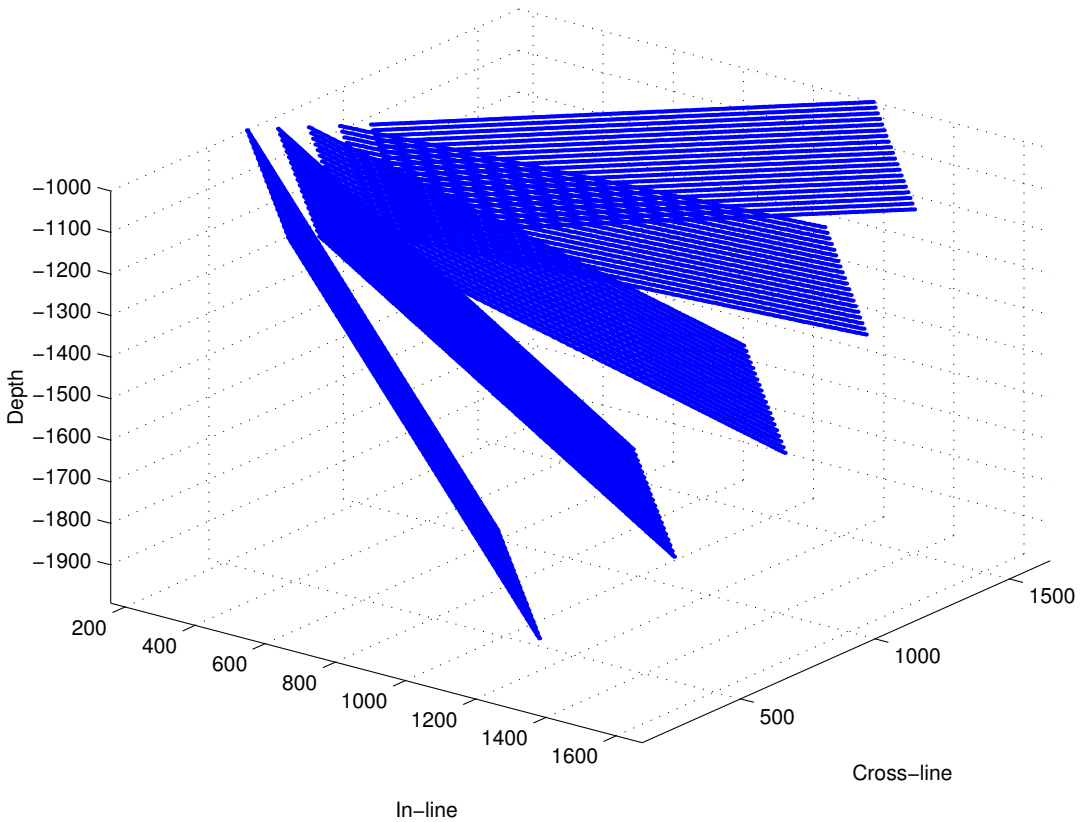

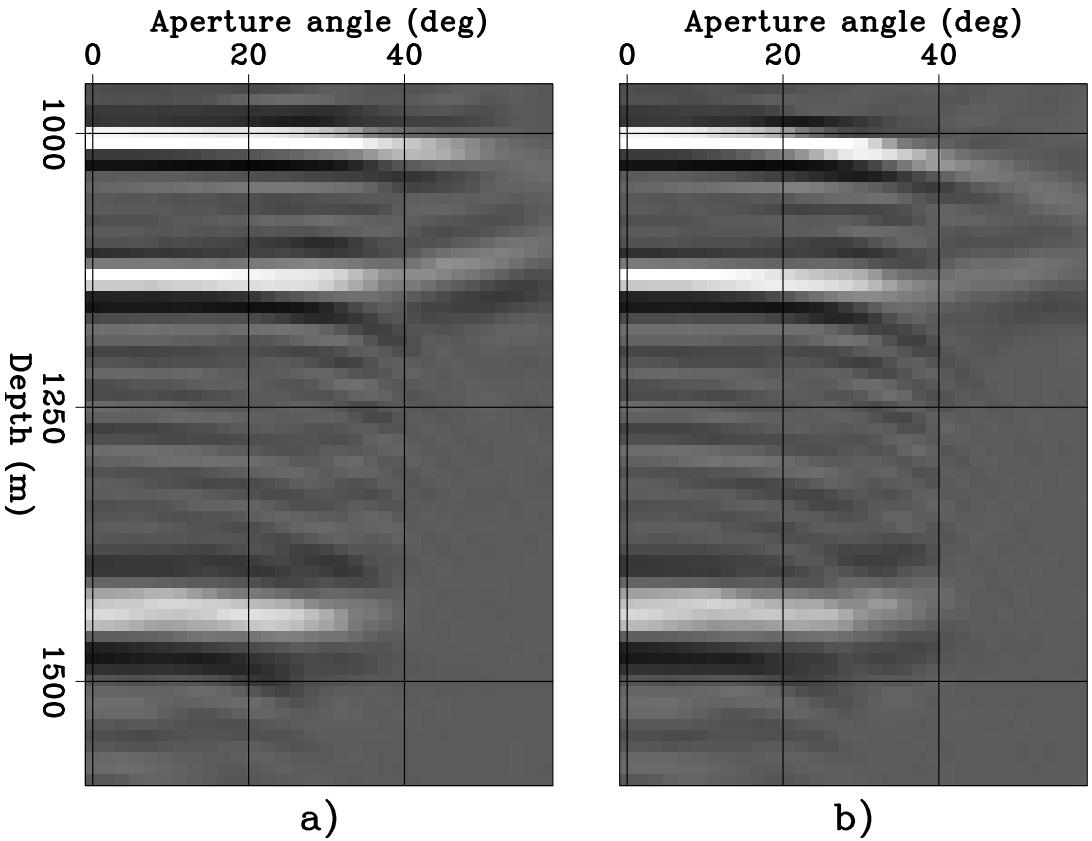

Figure 1.10: ADCIGs as functions of depth (z) and aperture angle (γ) for two different reflection azimuths and at constant horizontal location ($x = y = 450$ meters): $\phi = 10°$ (a), and $\phi = 15°$ (b). cig-cig-1-data8 [CR]

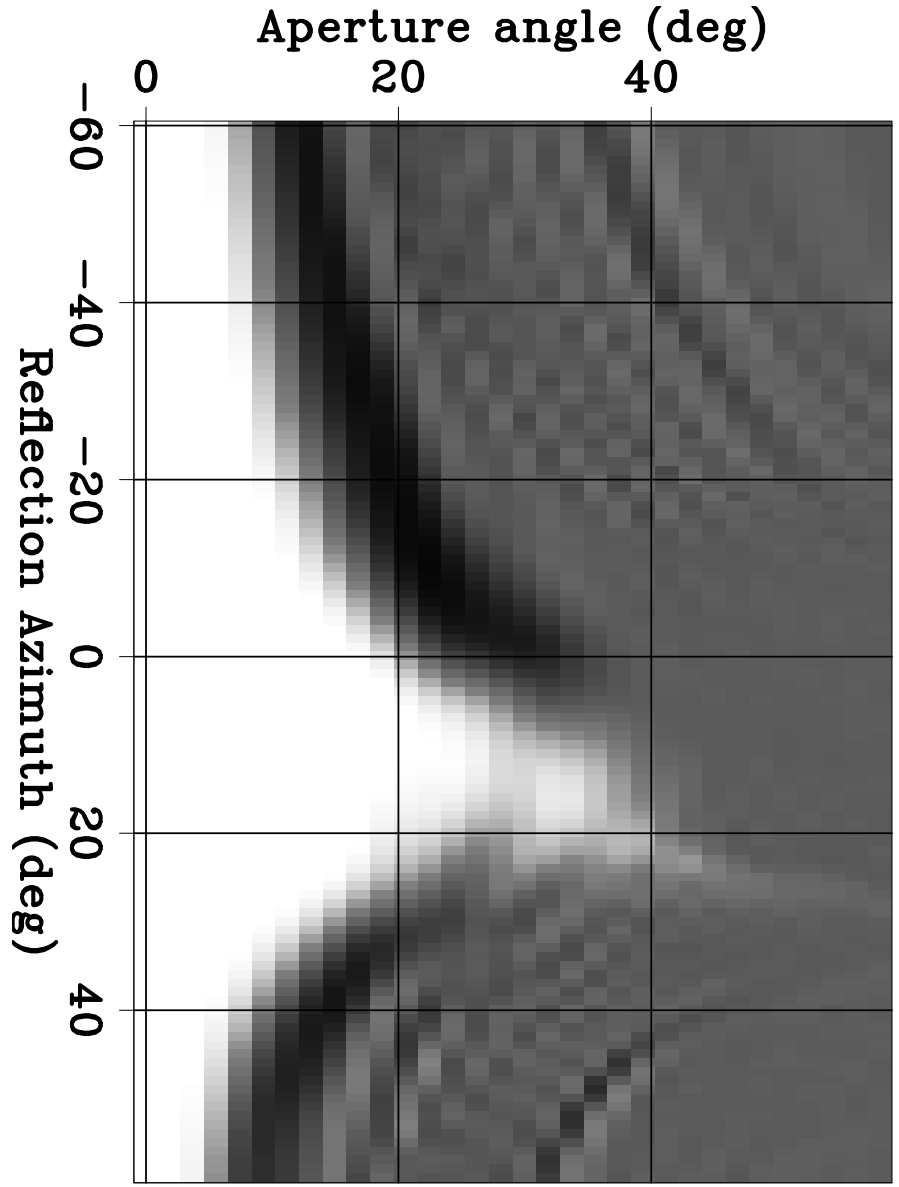

Figure 1.11: ADCIG as a function of aperture angle (γ) and reflection azimuth (ϕ) at constant depth ($z = 1{,}430$ meters) and horizontal location ($x = y = 450$ meters). cig-zaz-60-60-dense-all-v4-data8 [CR]

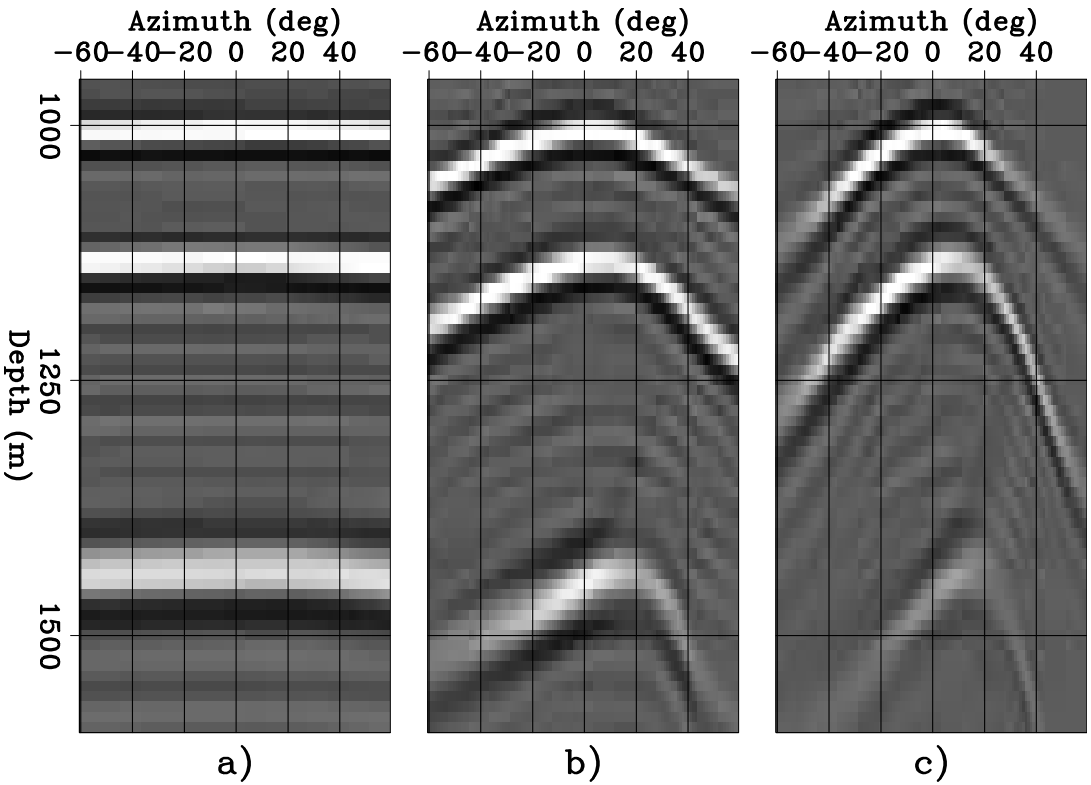

Figure 1.12: ADCIGs as functions of depth (z) and reflection azimuth (ϕ) for three different aperture angles and at constant horizontal location ($x = y = 450$ meters): $\gamma = 4°$ (a), $\gamma = 20°$ (b), and $\gamma = 30°$ (c). cig-azim-gamma-all-data8 [CR]

Outline

- Angle Domain Common Image Gathers (ADCIGs)
  - ADCIGs before imaging (2-D and 3-D)
  - ADCIGs after imaging (2-D and 3-D)
- ADCIGs and velocity errors
  - Image-point movement caused by velocity errors
  - 3-D Residual Moveout in angle domain
- Aliasing in prestack wave-equation migration
  - Operator aliasing in wavefield-continuation migration
  - Shot decimation in stack and ADCIGS
  - Aliasing and velocity estimation

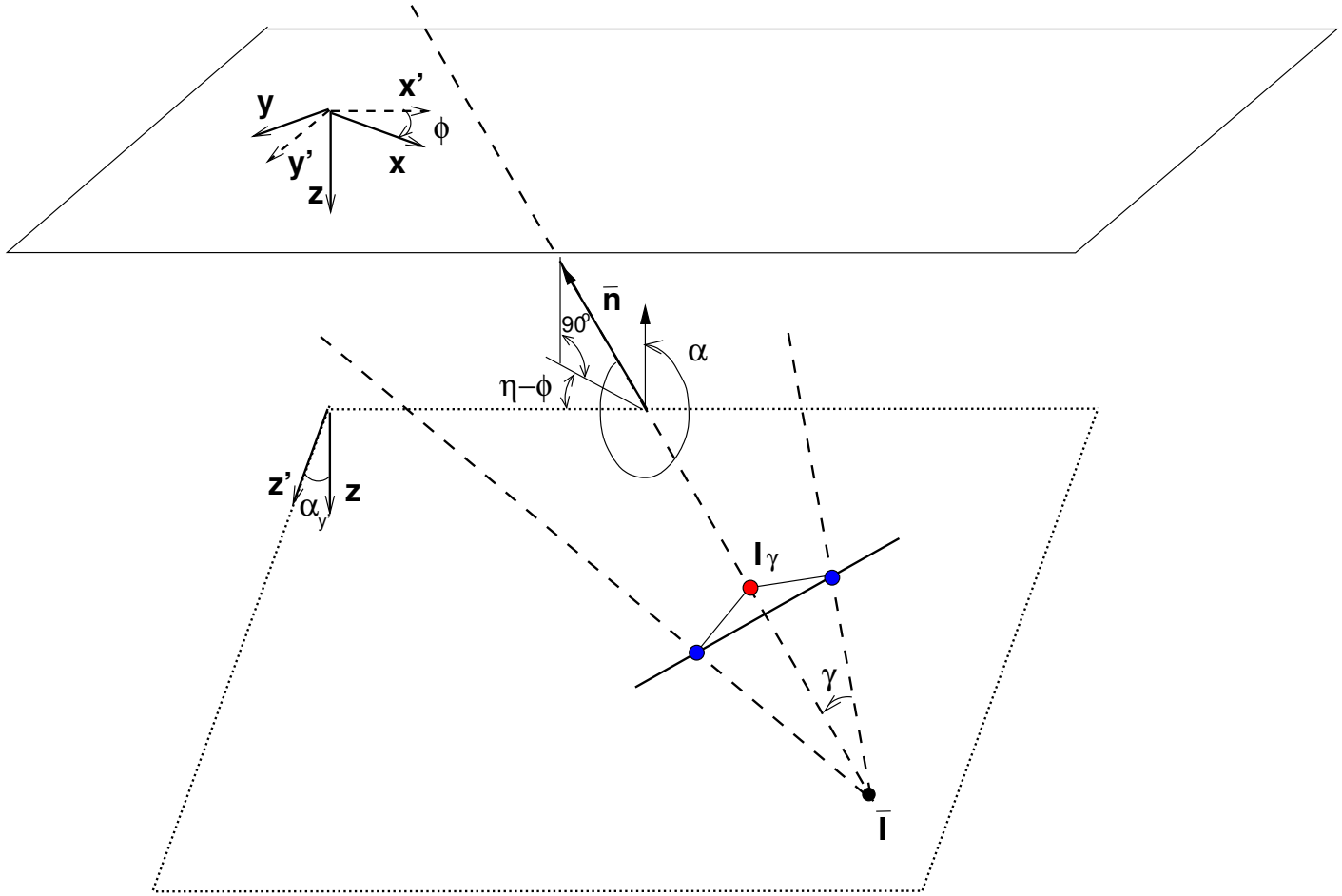

Figure 1.11: Geometry of an ADCIG for a single event migrated with the wrong velocity. The velocity error causes the shift of the image point from $\bar{\mathbf{I}}$ to $\mathbf{I}_\gamma$. Compare this figure with Figure **??**. migvel-cig-3d-mva-v6 [NR]

$p_{x's}, p_{y's}, p_{x'g}, p_{y'g}$ must be related by the following expression:

$$\left(p_{y'g} - p_{y's}\right) = \left(p_{y'g} + p_{y's}\right) \frac{\sqrt{\frac{1}{v^2(\mathbf{g}',z)} - p_{x'g}^2} - \sqrt{\frac{1}{v^2(\mathbf{s}',z)} - p_{x's}^2}}{\sqrt{\frac{1}{v^2(\mathbf{g}',z)} - p_{x'g}^2} + \sqrt{\frac{1}{v^2(\mathbf{s}',z)} - p_{x's}^2}}. \tag{1.9}$$

This relationship was derived by Biondi and Palacharla (1996) to define common-azimuth migration, and it is demonstrated in the Appendix of their paper.

Using the relationships among the ray parameters expressed in equations (**??**) and the relationships between the ray parameters and the angles expressed in equations (1.7), and after applying trigonometric identities, we can rewrite equation (1.9) as follows:

$$p_{y'h} = \frac{\sin\alpha_{y'}\left(\cos\beta_r - \cos\beta_s\right)}{v\left(z',x',y'\right)\left(\cos\beta_r + \cos\beta_s\right)} = -\frac{\sin\alpha_{y'}\tan\gamma\tan\alpha_{x'}}{v\left(z',x',y'\right)}. \tag{1.10}$$

The in-line offset ray parameter from equation (1.8) can also be rotated by the azimuth ϕ to give the following expression:

$$p_{x'h} = \frac{2\sin\gamma\cos\alpha_{x'}}{v\left(z',x',y'\right)}, \tag{1.11}$$

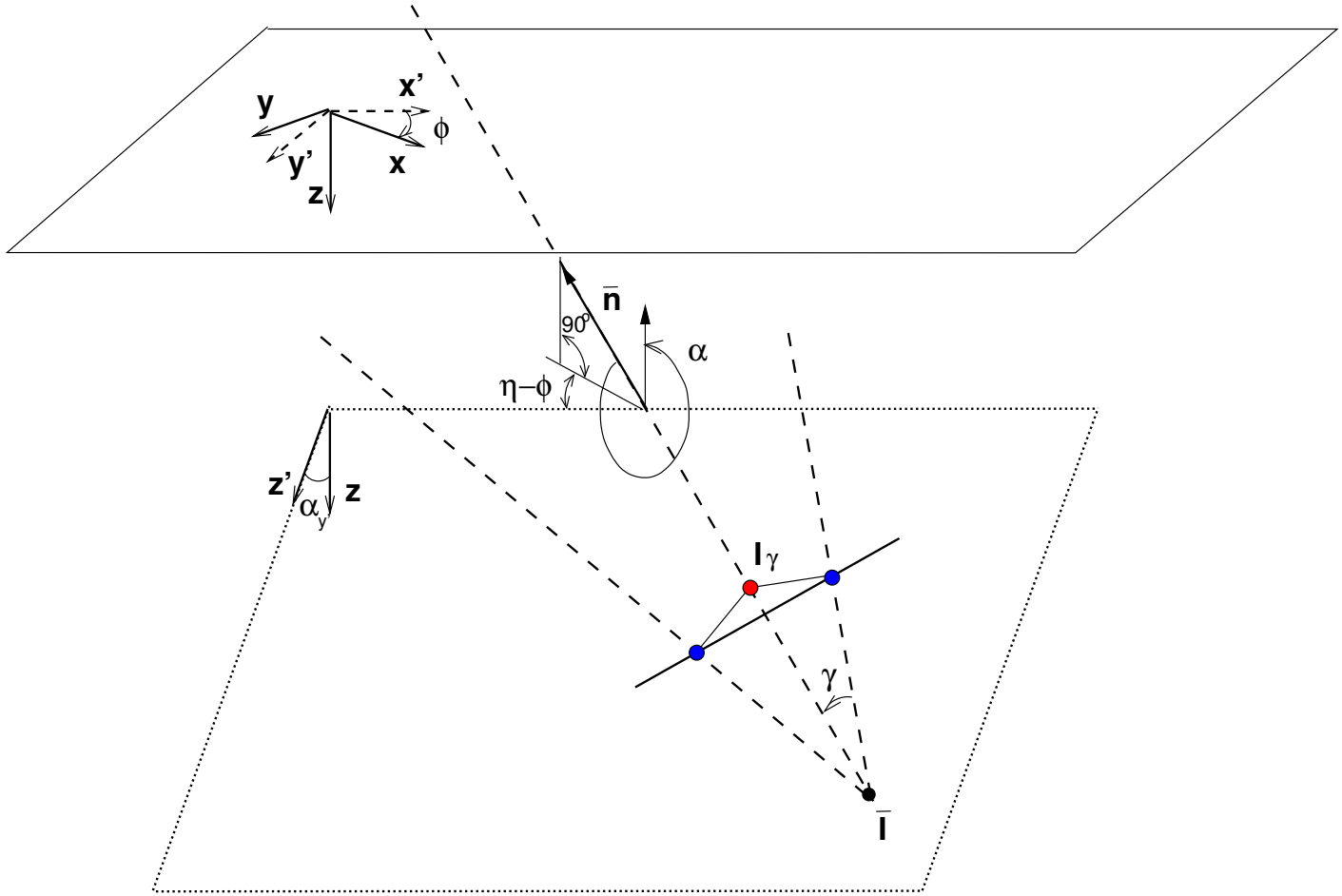

Figure 1.11: Geometry of an ADCIG for a single event migrated with the wrong velocity. The velocity error causes the shift of the image point from $\bar{\mathbf{I}}$ to $\mathbf{I}_\gamma$. Compare this figure with Figure **??**. migvel-cig-3d-mva-v6 [NR]

inclination of the tilted plane. In 3-D equation (1.10) becomes:

$$\begin{aligned}\Delta\mathbf{n}_{\mathrm{RMO}} &= \frac{\rho-1}{\cos\alpha_{x'}}\frac{\sin^2\gamma}{\left(\cos^2\alpha_{x'}-\sin^2\gamma\right)}z_0'\,\mathbf{n} \\ &= \frac{\rho-1}{\cos\alpha_x\cos\alpha_y}\frac{\sin^2\gamma}{\left(\cos^2\alpha_{x'}-\sin^2\gamma\right)}z_0\,\mathbf{n}. \end{aligned} \tag{1.12}$$

When $\alpha_{x'}$ and $\alpha_{y'}$ are available the RMO function could be directly evaluated using the expression in equation (1.12). However, in several situations it is more useful to express the RMO function explicitly as a function of the geological dip α, the azimuth angle of the normal to the geological dip η, and the azimuth angle of the reflected event ϕ (see Figure 1.11), with the following expression:

$$\Delta\mathbf{n}_{\mathrm{RMO}} = \frac{\rho-1}{\cos\alpha}\frac{\sin^2\gamma}{\left(1-\sin^2\alpha\cos^2(\eta-\phi)-\sin^2\gamma\right)}z_0\,\mathbf{n}. \tag{1.13}$$

Equation (1.13) is the general expression of the RMO function in 3-D.

In practice, it is computationally simpler to apply the RMO function at fixed surface location, that is as a vertical shift ($\Delta\mathbf{z}_{\mathrm{RMO}}$) instead as a normal shift ($\Delta\mathbf{n}_{\mathrm{RMO}}$).

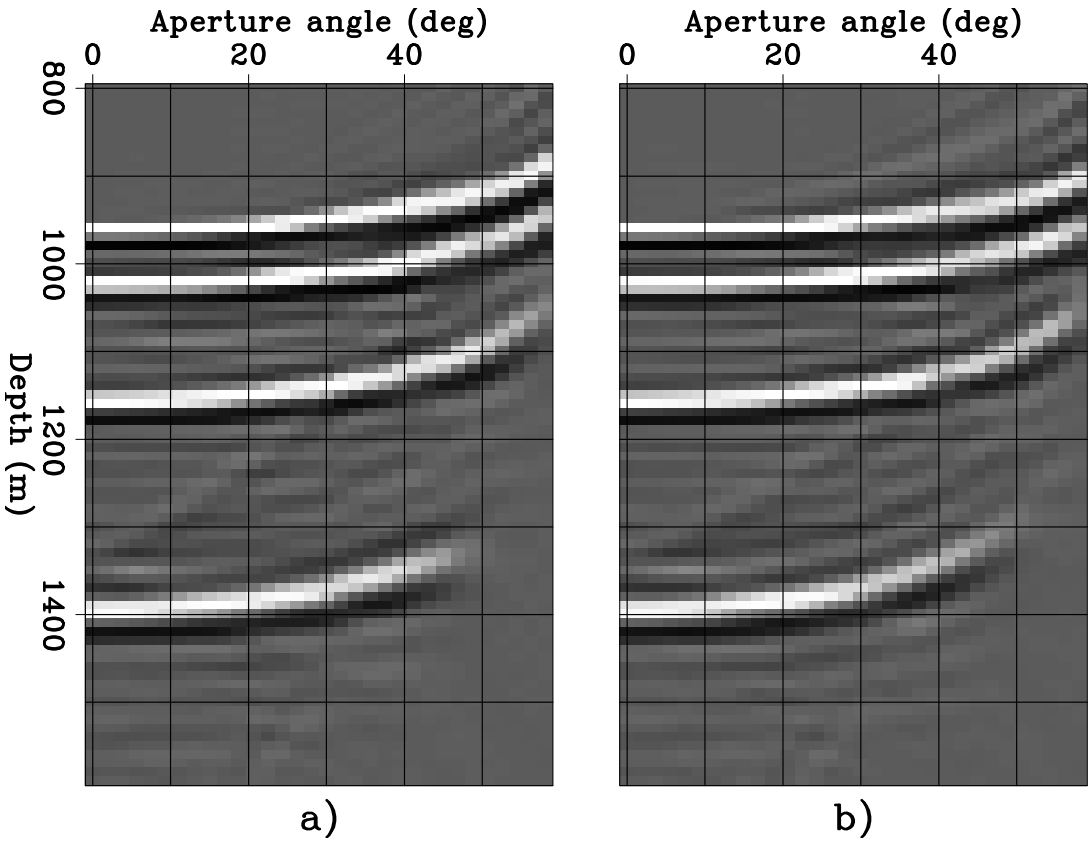

Figure 1.12: ADCIGs as functions of depth (z) and aperture angle (γ) for two different reflection azimuths and at constant horizontal location ($x = y = 700$ meters): $\phi = 0°$ (a), and $\phi = 7°$ (b). migvel-cig-2-data7 [ER]

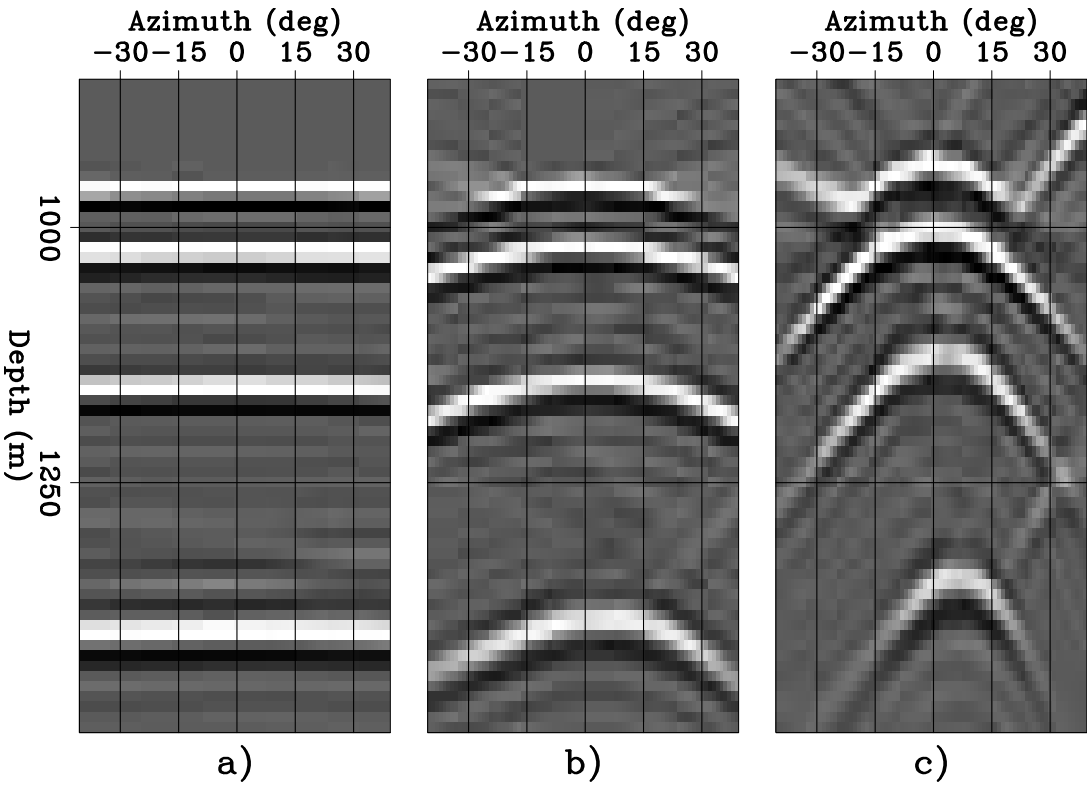

Figure 1.13: ADCIGs as functions of depth (z) and reflection azimuth (ϕ) for three different aperture angles and at constant horizontal location ($x = y = 700$ meters): $\gamma = 4°$ (a), $\gamma = 20°$ (b), and $\gamma = 40°$ (c). migvel-azim-gamma-all-data7 [ER]

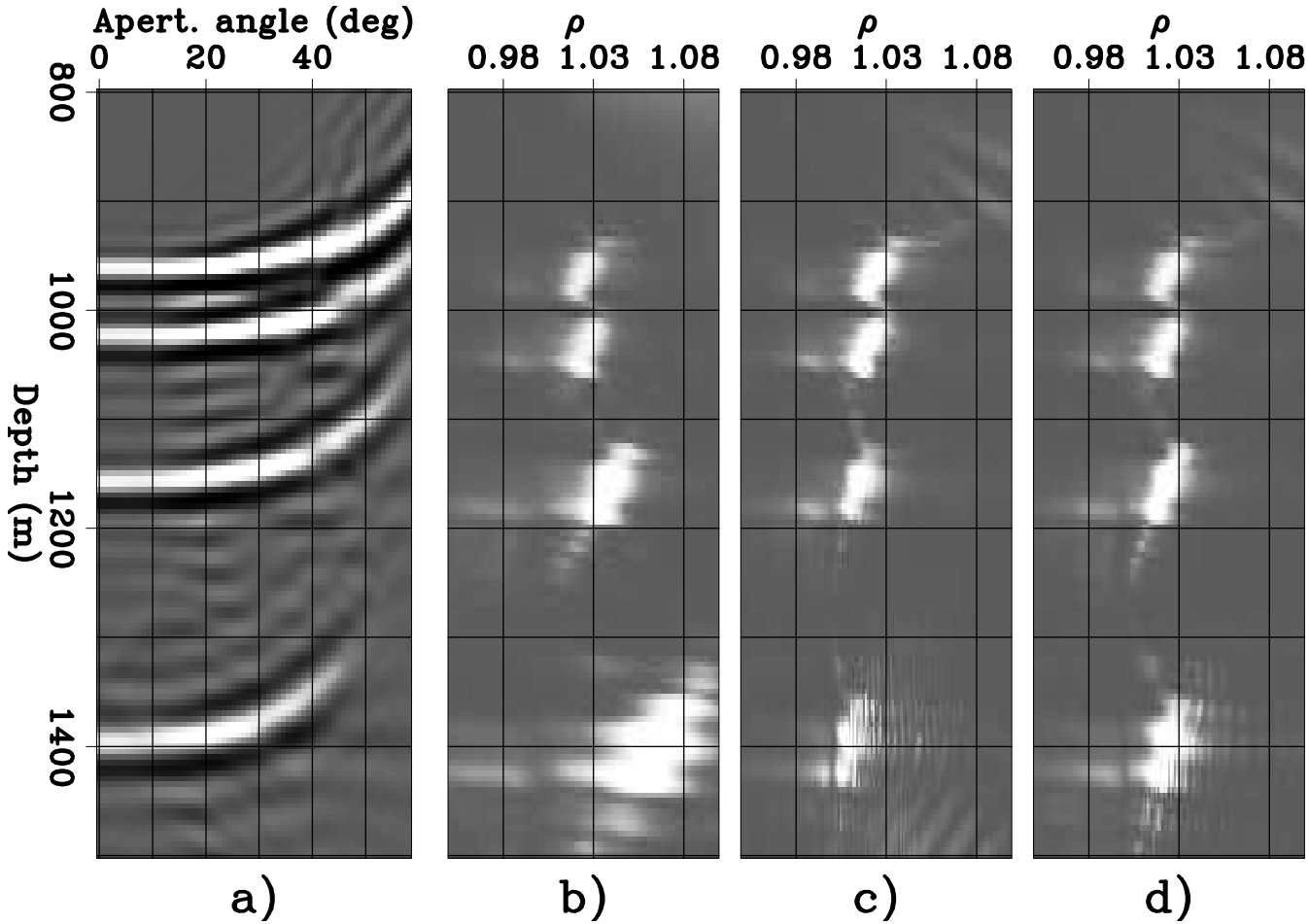

Figure 1.14: ADCIG and corresponding ρ-spectra computed using the 3-D RMO function in equation (1.13) with different set of parameters: $\alpha = 0$ (b), $\eta = \phi$ (c), $\eta = 45^o$ and $\phi = 0^o$ (d). migvel-zg_zs_zsa-overn [ER]

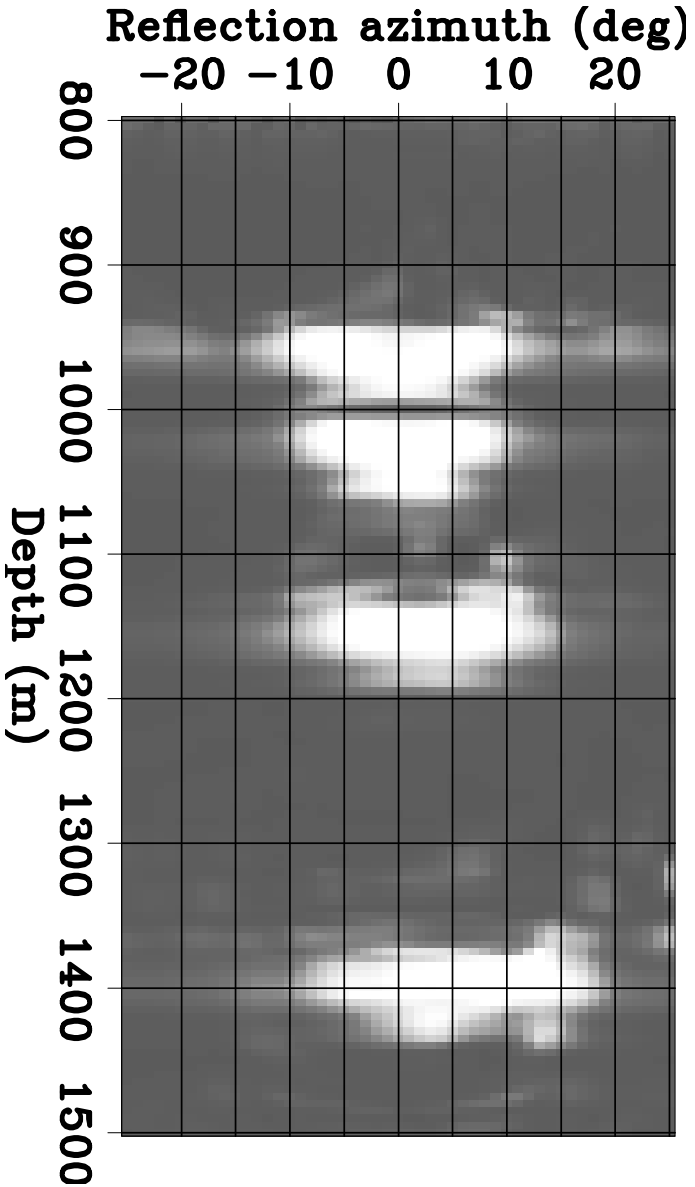

Figure 1.15: Semblance plot used to estimated the apparent reflection azimuth of reflections. For each reflector, the position of the semblance peaks correspond to the estimated reflection azimuth. migvel-pfan-overn [ER]

Outline

- Angle Domain Common Image Gathers (ADCIGs)
  - ADCIGs before imaging (2-D and 3-D)
  - ADCIGs after imaging (2-D and 3-D)
- ADCIGs and velocity errors
  - Image-point movement caused by velocity errors
  - 3-D Residual Moveout in angle domain
- Aliasing in prestack wave-equation migration
  - Operator aliasing in wavefield-continuation migration
  - Shot decimation in stack and ADCIGS
  - Aliasing and velocity estimation

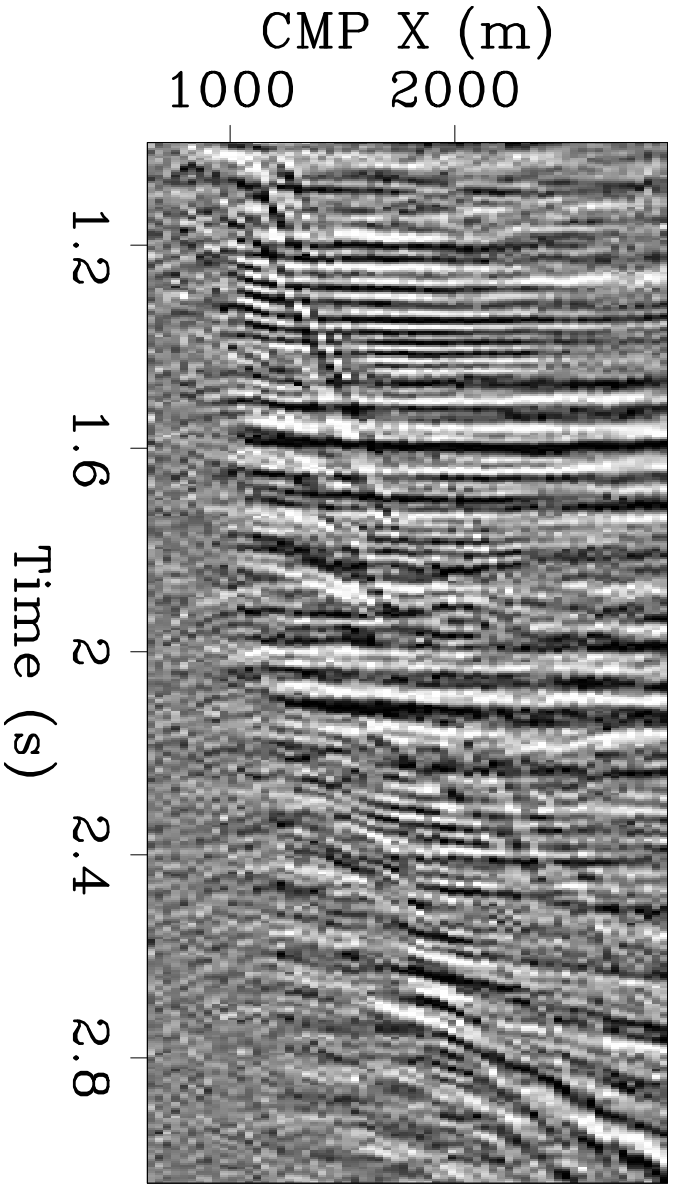

Figure 1.5: Data window containing aliased reflections from the salt flanks. alias-Wind-data [ER]

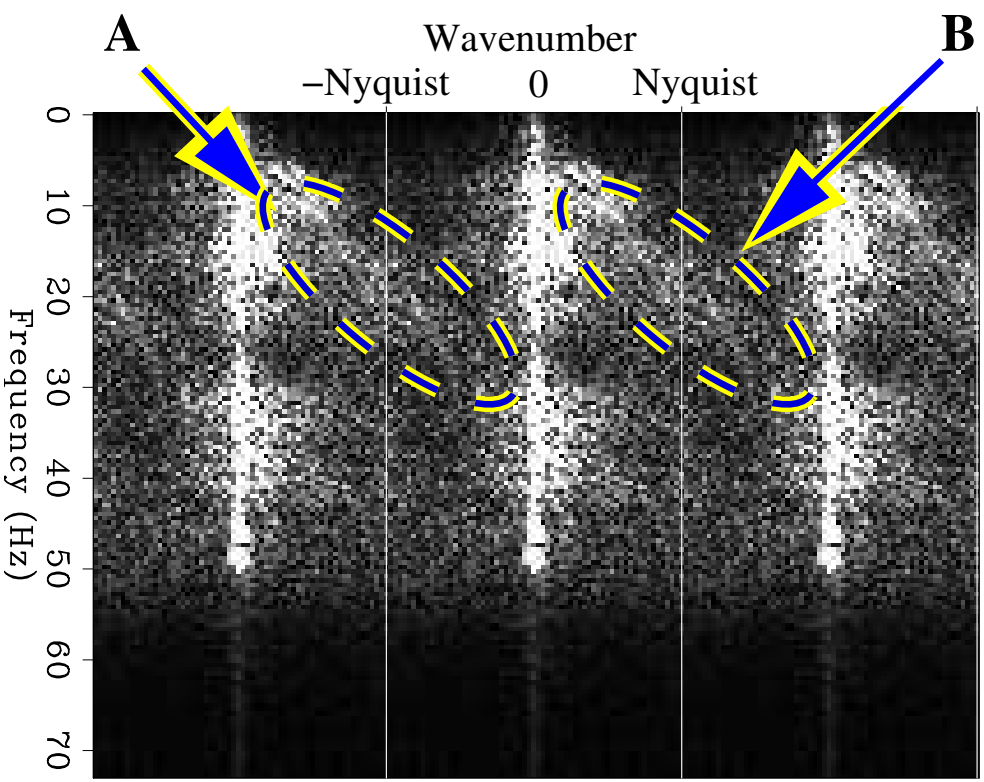

Figure 1.6: Frequency-wavenumber spectrum of the data window shown in Figure 1.5. Notice that the aliased events correspond to the "clouds" in the spectrum contoured with ellipses in the Figure. The ellipse marked as **B** contours the energy that can be correctly migrated. The ellipse marked as **A** contours the energy that cannot be correctly migrated and should be avoided during the summation. alias-Wind-spec-geo2 [NR]

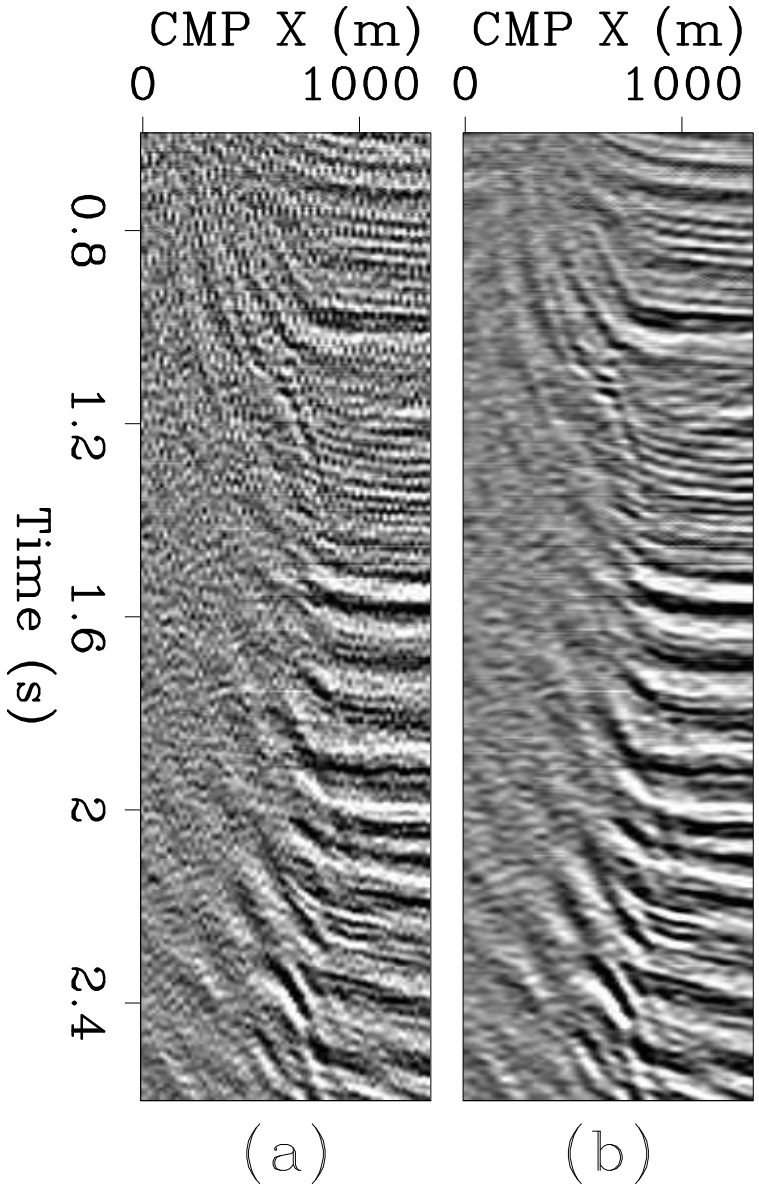

Figure 1.3: 3-D migrations of salt-dome flanks in the Gulf of Mexico: (a) migration obtained without the use of any anti-aliasing filter, (b) migration obtained with the application of a "standard" anti-aliasing filter. alias-Comp-WL-intro [ER]

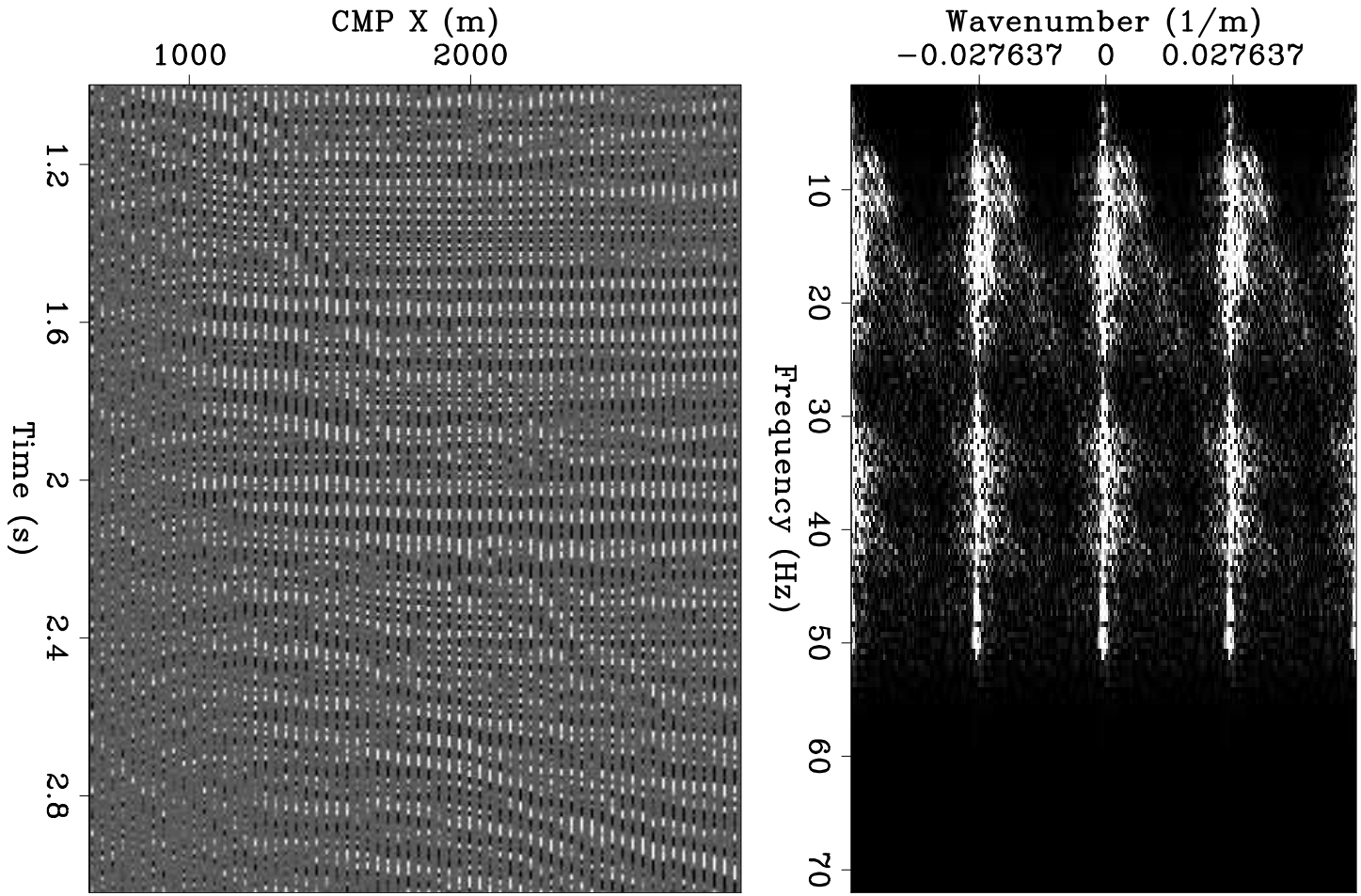

Figure 1.1: Same data window of the Gulf of Mexico data shown in Figure **??**, but with three zero traces inserted for each live trace (left panel), and frequency-wavenumber spectrum of the interleaved data (right panel). alias-Wind-comb-data-spec [ER]

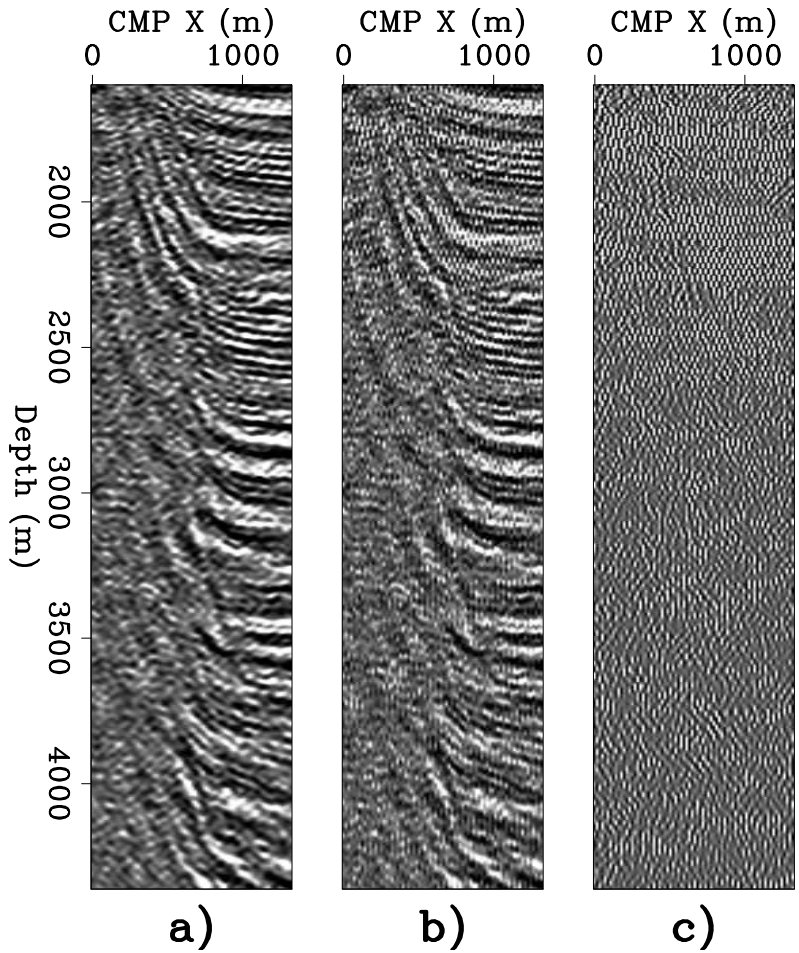

Figure 1.2: Images obtained by performing zero-offset downward-continuation migration: on the data obtained by interpolating the original data on a grid four times finer (a), on the data obtained by interleaving the original data with three zero traces for each live trace (b), and difference between panel a) and panel b) (c). alias-Mig-interp-comb-diff-overn [ER]

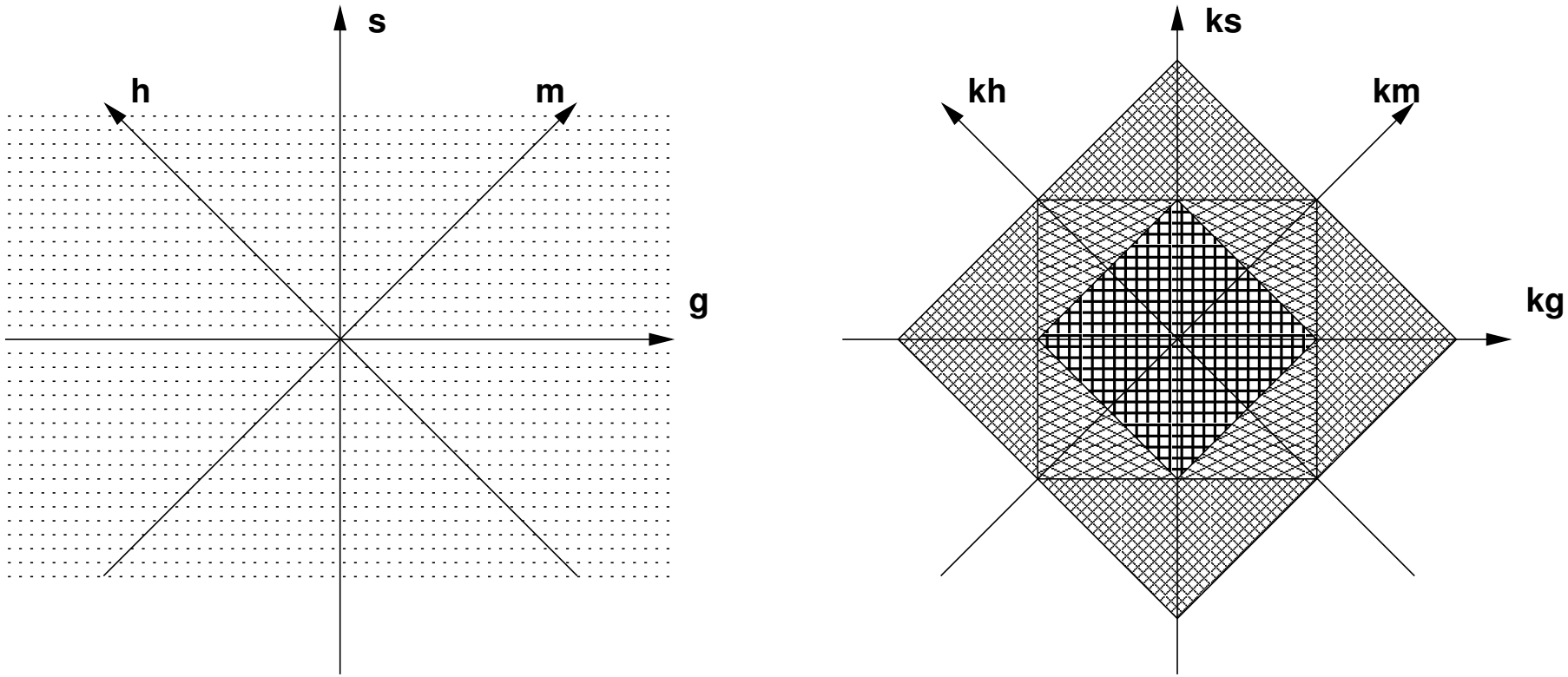

Figure 1.3: Graphical representation of a data set with $\Delta_s = \Delta_g$ in the space domain (left panel), and wavenumber domain (right panel). In the right panel, the inner square represents the data set in the midpoint-offset wavenumber domain with $\Delta_m = \Delta_h = \Delta_s$. The middle square represents the data set in the source-receiver wavenumber domain with $\Delta_s = \Delta_g$. The outer square represents the data set in the midpoint-offset wavenumber domain with $\Delta_m = \Delta_h = \Delta_s/2$. alias-sr-basic-v2 [NR]

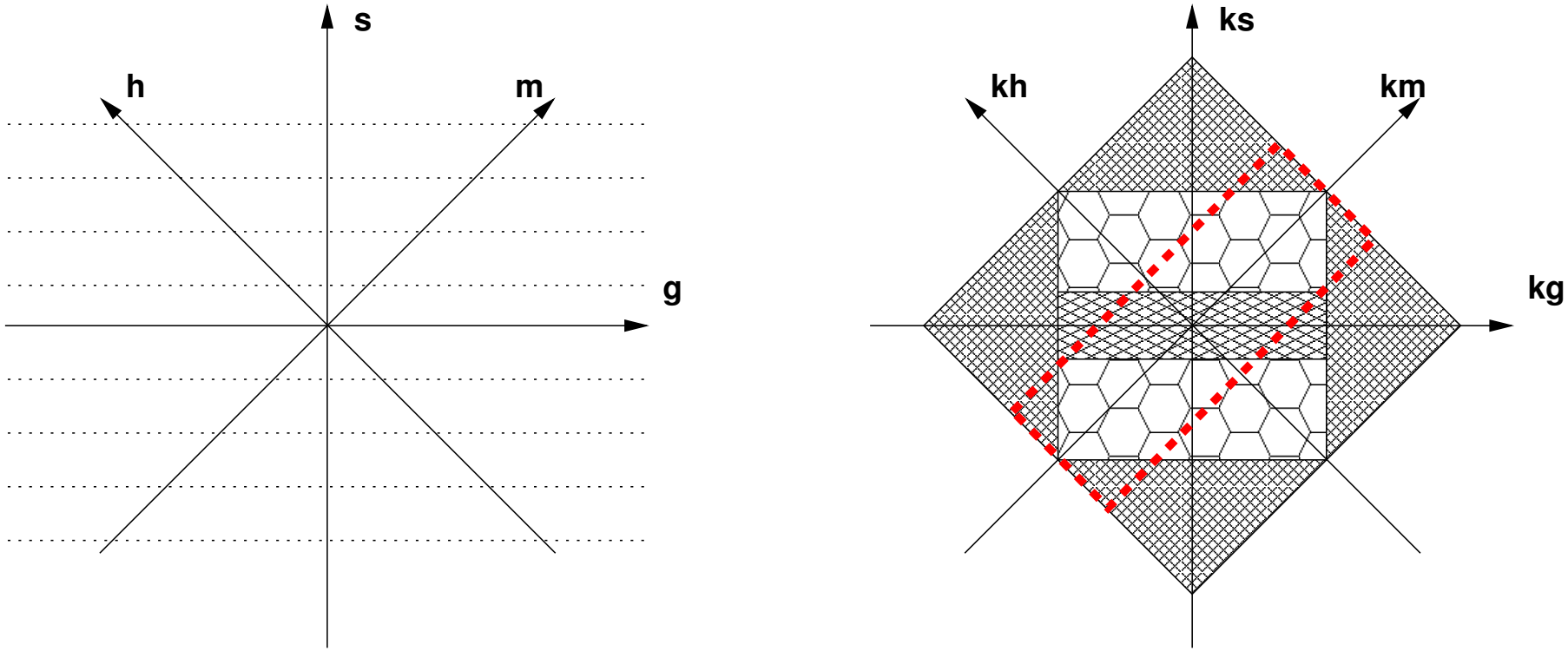

Figure 1.4: Graphical representation of a data set with $\Delta_s = 4\Delta_g$ in the space domain (left panel), and wavenumber domain (right panel). In the right panel, the middle rectangle represents the main band of the data set in the source-receiver wavenumber domain with $\Delta_s = 4\Delta_g$. The areas filled with an hexagonal pattern are the side bands along the source wavenumber axis. The dashed box indicates the area contributing to the image when the antialiasing procedure described in the text is applied. alias-sr-under-v2 [NR]

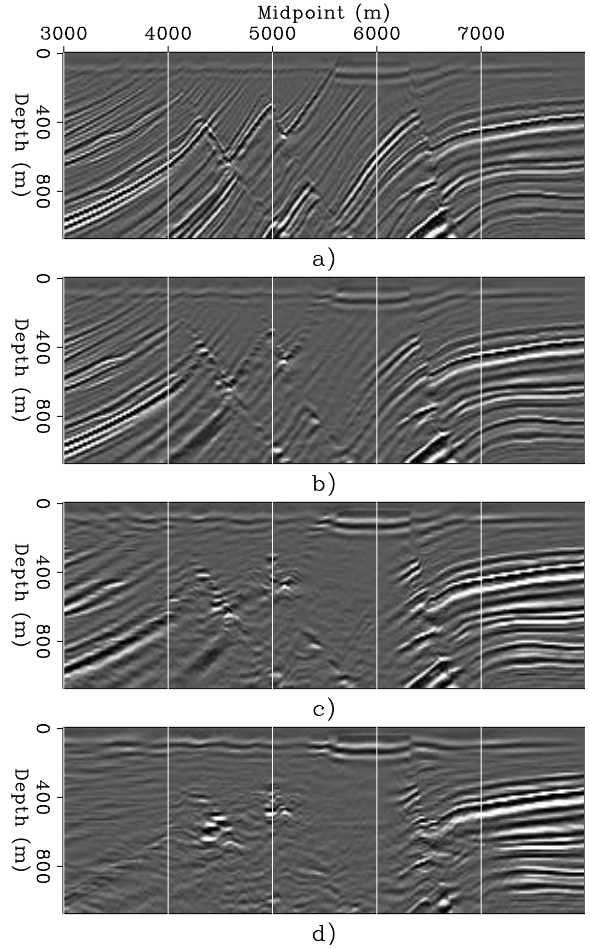

Figure 1.5: The panel on the top displays the migrated section obtained by using all the shots in the data ($\Delta_s = 25$ meters). The other migrated sections are obtained by decimating the shots, followed by interleaving the decimated shots with zero traces along the shot axis, and then bandpassing along the source axis before migration. The shots interval were: $\Delta_s = 50$ meters for panel b), $\Delta_s = 100$ meters for panel c), and $\Delta_s = 200$ meters for panel d). alias-zoff-all-bpass-overn [ER]

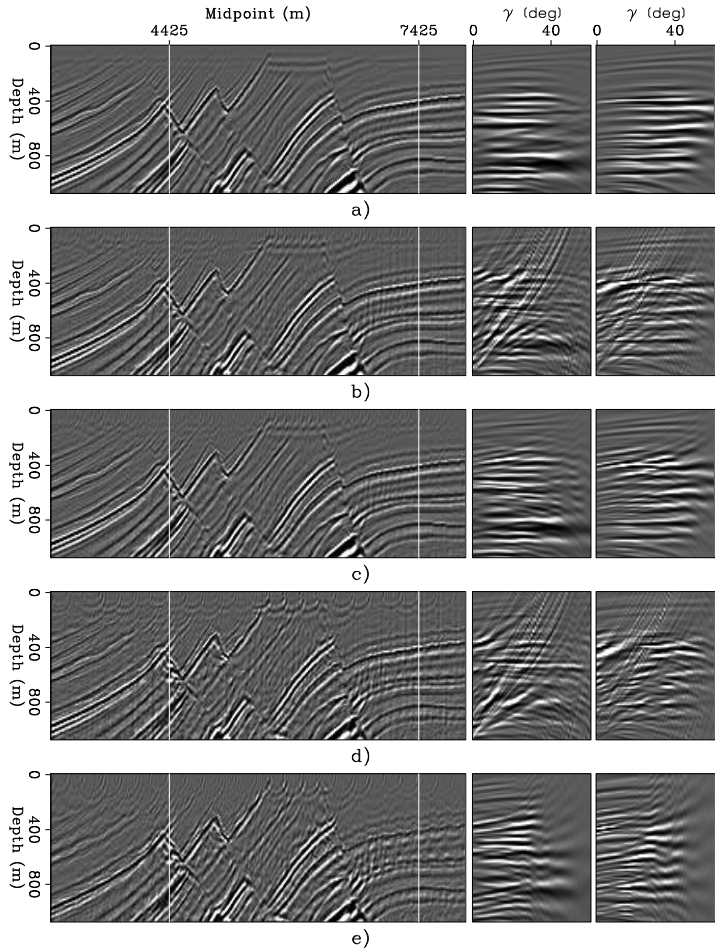

Figure 1.6: The panel on the top displays the migrated section and two ADCIGs obtained by using all the shots in the data ($\Delta_s = 25$ meters). The other migrated results are obtained by first decimating the shots and then interleaving the decimated shots with zero traces along the shot axis. The shots interval were: $\Delta_s = 100$ meters for panel b) and c), and $\Delta_s = 200$ meters for panel d) and e). alias-zoff-cig-all-overn [ER]

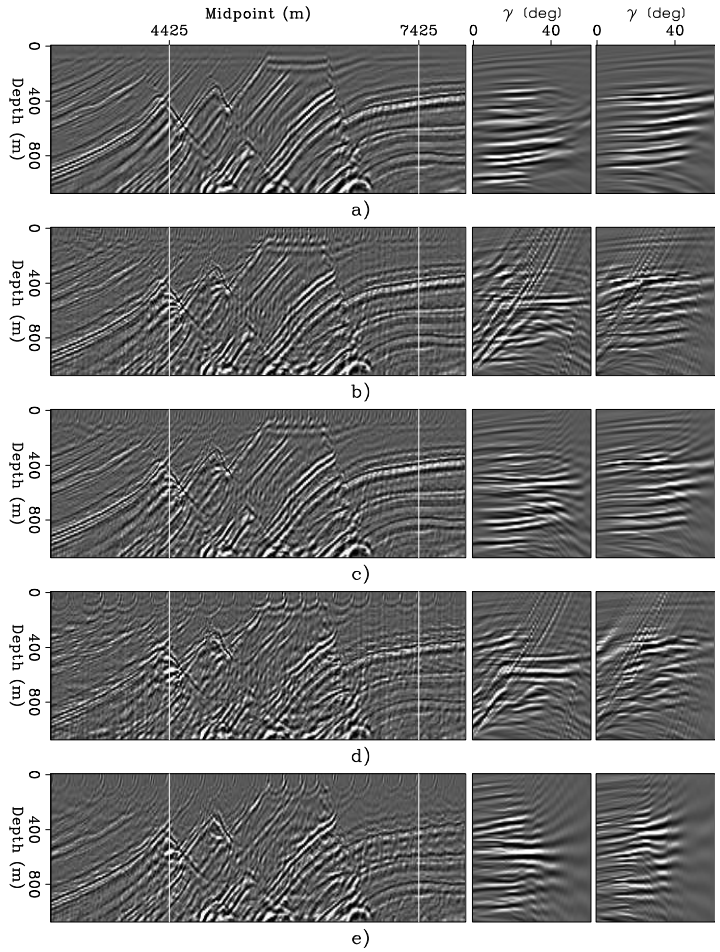

Figure 1.7: The panel on the top displays the migrated section and two AD-CIGs obtained by using all the shots in the data ($\Delta_s = 25$ meters). The other migrated results are obtained by first decimating the shots and then interleaving the decimated shots with zero traces along the shot axis. The shots interval were: $\Delta_s = 100$ meters for panel b) and c), and $\Delta_s = 200$ meters for panel d) and e). alias-zoff-cig-all-slow-overn [ER]